Rev. Brasil. Apl. Vac., Vol 6, nºs 1 e 2,1986

ION BEAM SPUTTERED ITO AS A WINDOW LAYER MATERIAL FOR PHOTOVOLTAIC APPLICATIONS

T.J. Coutts, T.A. Gessert, R.G. Dhere,
A.J. Nelson and H. Aharoni*

Solar Energy Research Institute
1617 Cole Blvd.
Golden, Colorado 80401 USA

*On leave from Ben Gurion University of
the Negev, Beer-Sheva, Israel

This work has been concerned with the measurement and analysis of the electro-optical properties of thin films of indium tin oxide deposited by ion-beam sputtering. In the present context the principal use of these films is for window layer solar cells and it is necessary to have an accurate knowledge of the optical and electrical properties, and their dependence on deposition conditions, to enable realistic predictions of the internal quantum efficiency to be made. We have measured the properties of films as a function of deposition rate, partial pressure of oxygen in the sputtering gas, and annealing temperature. The properties studied are the variation with wavelength of the optical constants, the Hall mobility, the film structure and composition.

The compositional data (XPS) suggest that heat treatment causes the Sn to substitute for In atoms, and hence to act as singly ionized donors. Films deposited in a low partial pressure of oxygen also have double ionized oxygen vacancies. Estimates of the free carrier density have been made using XPS measurements of the Sn content and the atomic deficiency of oxygen. Comparison with the measured values gives reasonable agreement. Films deposited in a relatively high partial pressure of oxygen show a very low carrier concentration before heat treatment. However, in this case also, heating to about 350-400°C causes an increase in the free carrier concentration to about the same level as for films with a near stoichiometric oxygen content. This demonstrates the role of excess oxygen as an electron trap.

Oxygen deficient films which have not been annealed exhibit a mobility which appears to be limited by grain boundary and ionized impurity scattering. After annealing (and the consequent grain growth) the mobility is limited only by ionized impurity scattering. Oxygen rich films which have not been annealed exhibit a mobility which is limited only by grain boundary scattering. After annealing, these also are limited by ionized impurities only. The minimum resistivity achievable therefore appears to depend upon the unavoidable interaction between carrier concentration and mobility.

From the optical data it is shown that the optical gap varies with the free carrier concentration according to the Moss-Burstein effect. In the near IR, the films exhibit a plasma absorption edge in accordance with the Drude free carrier model.

Indium Tin Oxide, Ion Beam Sputtered, Electro-Optical Properties

Introduction

The family of transparent conductors, particularly indium-tin oxide (ITO), has found widespread application in recent years and a large volume of literature has ensued. For a general overview of the topic, the recent review of Chopra et al (1) is recommended. Both single crystals and thin films have been investigated and one of the major interests has been to achieve electronic mobilities in thin films as large as those in single crystals. The explanations of the difference in mobility involve various mechanisms, such as ionized impurity (2), electron/electron (3), and grain boundary (4), scattering although only the latter would be specific to thin films. As we shall see later, the electronic mean free path is usually comparable with the typical grain size for unannealed films and we would therefore expect grain boundaries to play a significant role.

The films have been deposited by a wide range of techniques and have exhibited remarkably similar properties even though there are several fabrication parameters to which the properties would be expected to be sensitive (substrate temperature, oxygen partial pressure, post-deposition annealing, source composition, being the most commonly investigated). Likewise, the variation of many physical properties with the fabrication parameters has been studied and models of the electronic structure have been developed. Nevertheless, a thorough understanding

of the material does not exist and the reasons for the existence of a lower limit to the resistivity are not at all obvious. For some applications, e.g. displays, the lower limit of about 10^{-4} Ω-cm is not problematic but for window-layer solar cells it is highly desirable to minimize the sheet resistance since this leads to a reduction of the grid shadowing loss. However, it is also vital that the optical transmittance is maximized and the trade-off between these factors has led to the 'figure-of-merit' (5) concept. Whilst this may be of value for certain applications, it is not really useful if one is attempting to model the variation of the quantum efficiency of a solar cell with wavelength. In this case the variation of the optical constants $N(\lambda)$ and $k(\lambda)$ is required to be known so that the number of photons actually transmitted into the active semiconductor can be calculated. This is vital if accurate device modelling is to be performed. For example, it is known that the optical gap of ITO varies with the density of free carriers through the Moss-Burstein effect, and it is necessary to determine whether the short wavelength cut-off of devices utilizing ITO window layers (e.g., ITO/InP, ITO/Si) is due to absorption in the ITO or to near surface effects in the absorber. There is also evidence of optical inhomogeneity (6) in the thickness of films which could impair performance of solar cells and lead to complications in the calculation of optical losses. Finally, instabilities in the opto-electronic properties have been observed and these are clearly undesireable from the point-of-view of the solar cell designer. In previous studies on RF sputtered ITO/InP cells (7), we have pointed out that the highest values of open-circuit voltage are achieved when the deposition rate of the ITO is extremely slow (0.2-0.3 Å s^{-1}) and the substrates are not heated above 150°C before, during or after deposition. These are unusual constraints on the deposition parameters and part of our objective of undertaking the present study was to determine their influence on $N(\lambda)$, $k(\lambda)$, the sheet resistance ($R_{\square}$), and the film stability, with a view to improving device performance. Additionally, as part of a continuing study on the nature of the ITO/InP cell (8), we are depositing the ITO by ion-beam sputtering and detailed information on ITO prepared in this way is not readily available.

Hence, to summarize, our objectives in undertaking this work were as follows:

i) To determine the optical and electrical characteristics of ion-beam sputtered ITO, deposited at the very slow rates used in the fabrication of certain devices.

ii) To contribute to the volume of information on the fundamental properties of ITO and, in particular, to investigate the role of tin.

iii) To determine the nature of the scattering processes responsible for limiting electron mobilities and placing a lower limit of about 10^{-4} Ω-cm on resistivity.

To help elucidate these issues we have measured the Hall mobility, carrier density, dispersion of N and k, and the optical gap; assessment of the crystallinity has been made using X-ray diffraction, of the structure by electron microscopy and of the composition using X-ray photo-electron spectroscopy (XPS) and Mössbauer spectroscopy. These measurements have been made on films deposited at two rates, six different partial pressures of oxygen, and six annealing temperatures.

Experimental

The films were deposited in a Perkin-Elmer ULTEK ion-beam sputtering system which could achieve a base pressure in the range of $5-8\times10^{-7}$ torr using an Air Products cryo-pump (Model HV-202-6). After achieving the base pressure, the system was back-filled with ultra-pure argon (Linde Specialty Gases) to a pressure of 1×10^{-4} torr. A controlled amount of oxygen (Electronic Grade, Scientific Gas Products) was then added to produce the desired partial pressure (P_{O_2}). Then, with the substrate facing away from the target (91 m/o In_2O_3; 9 m/o SnO_2, supplied by MRC Inc., 5" diameter) the latter was pre-sputtered for 15 minutes under the same ion-beam parameters and the same oxygen partial pressure as used for the subsequent film deposition.

Two types of substrates were used in this work; for the optical, electrical, and X-ray diffraction analyses, Commercial Quality Quartz (Co-Quartz, supplied by ESCO Inc.) was used; for ellipsometric and XPS analyses, the substrates were single crystal silicon. In each deposition, 8 substrates were used (6 silicon and 2 quartz). The silicon was cleaved and ultrasonically degreased in trichloroethylene, acetone and isopropyl alcohol (all semiconductor grade organics). It was then etched by standard procedures using a solution of $5H_2SO_4:1H_2O_2$ followed

by rinsing in 18 Mega-Ohm deionized water. Finally, it was etched in a solution of $1HF:1H_2O$ and blown dry with ultra high purity nitrogen gas immediately before loading into the deposition system. The quartz substrates were similarly degreased and blown dry. All 8 substrates were held in a single holder which was rotated parallel so as to face the target after the latter had been pre-sputtered. Deposition was performed using an accelerating voltage, V_b, of 800 V and a beam current, I_b, of 30 mA (0.2-0.4 $\dot{A}\ s^{-1}$) or V_b = 1200V, I_b = 50 mA (0.6 - 0.9 $\dot{A}\ s^{-1}$). A thermocouple was used to monitor the approximate substrate temperature during deposition and it was found that this did not exceed 50°C. The film thickness always lay in the range of 650-750 A, depending on the oxygen partial pressure. After cooling and removal from the vacuum system, one of the films on a silicon substrate was used for thickness measurement. This was done by ellipsometry using a Rudolf Research Ellipsometer, at a wavelength of 6328 A. To make this measurement, it was necessary to assume a value of k at this wavelength. This was taken as 0.005, although later measurements by spectrophotometry demonstrated some variation depending on the preparation conditions. However, the error caused in the thickness and the real part of the refractive index, N, is negligible in this region of the spectrum where the films are essentially non-absorbing. For measurement of the free carrier density, n, and mobility, μ, a Hall probe was used and contact to one of the ITO films on quartz was made with indium wire pressure contacts. The flux density of the magnet was 5 k Gauss. n and μ were measured before each heat treatment step (see below). A Beckmann Spectrophotometer (Model No. 5240) was used to measure the reflectance at the air/ITO and air/quartz interfaces, and the total transmittance. The data were recorded automatically and stored in an HP 1000 computer for processing. Between 240-800 nm, the data were recorded at intervals of 1 nm; between 800-2500 nm they were recorded every 4 nm. The use of automated data acquisition also permitted the base line and 100% line of the spectrophotometer to be recorded, and the optical constants of the quartz substrates to be stored. Since the derived values are quite sensitive to relatively small variations in the measured optical quantities, a smoothing routine was used to reduce irregularities in the data. The film used for optical analysis was also used subsequently for X-ray diffraction. X-ray diffraction analysis was performed on a Rigaku X-ray diffractometer with rotating anode (Model Ru-200V) using Cu-K_α radiation at 40 kV and 100 mA.

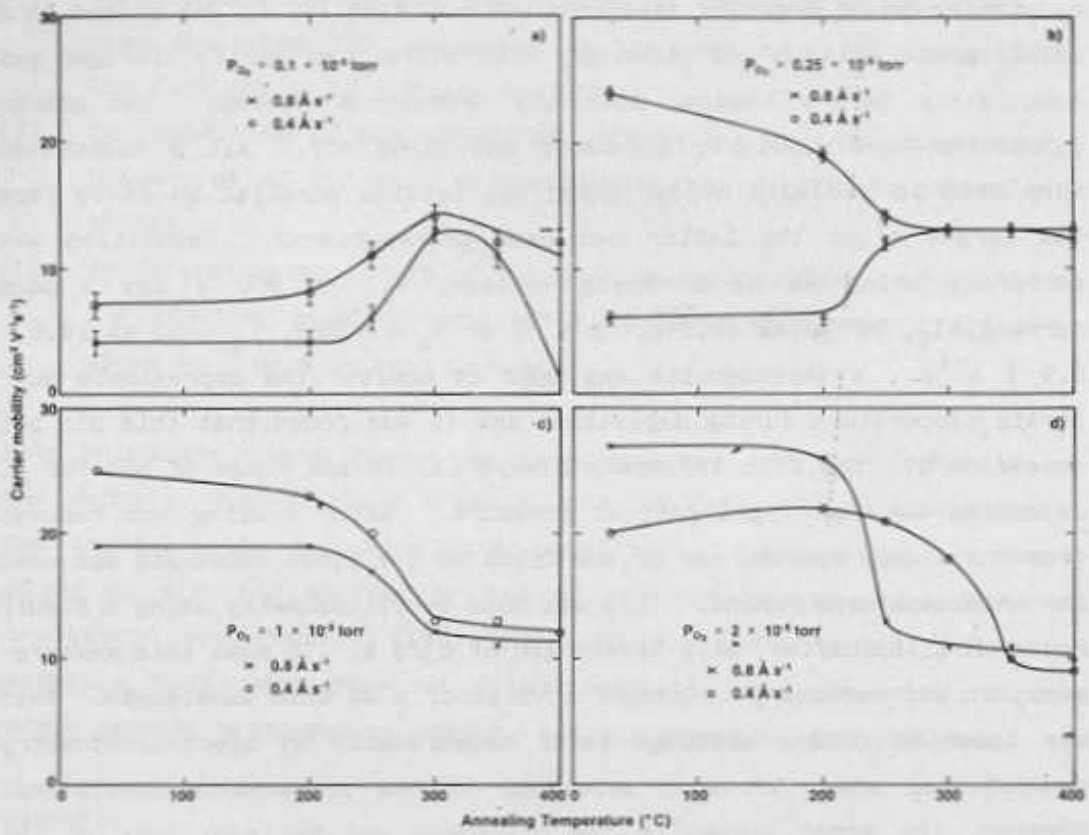

Fig. 1 a-e: Carrier mobility against annealing temperature for various partial pressures of oxygen and deposition rates.

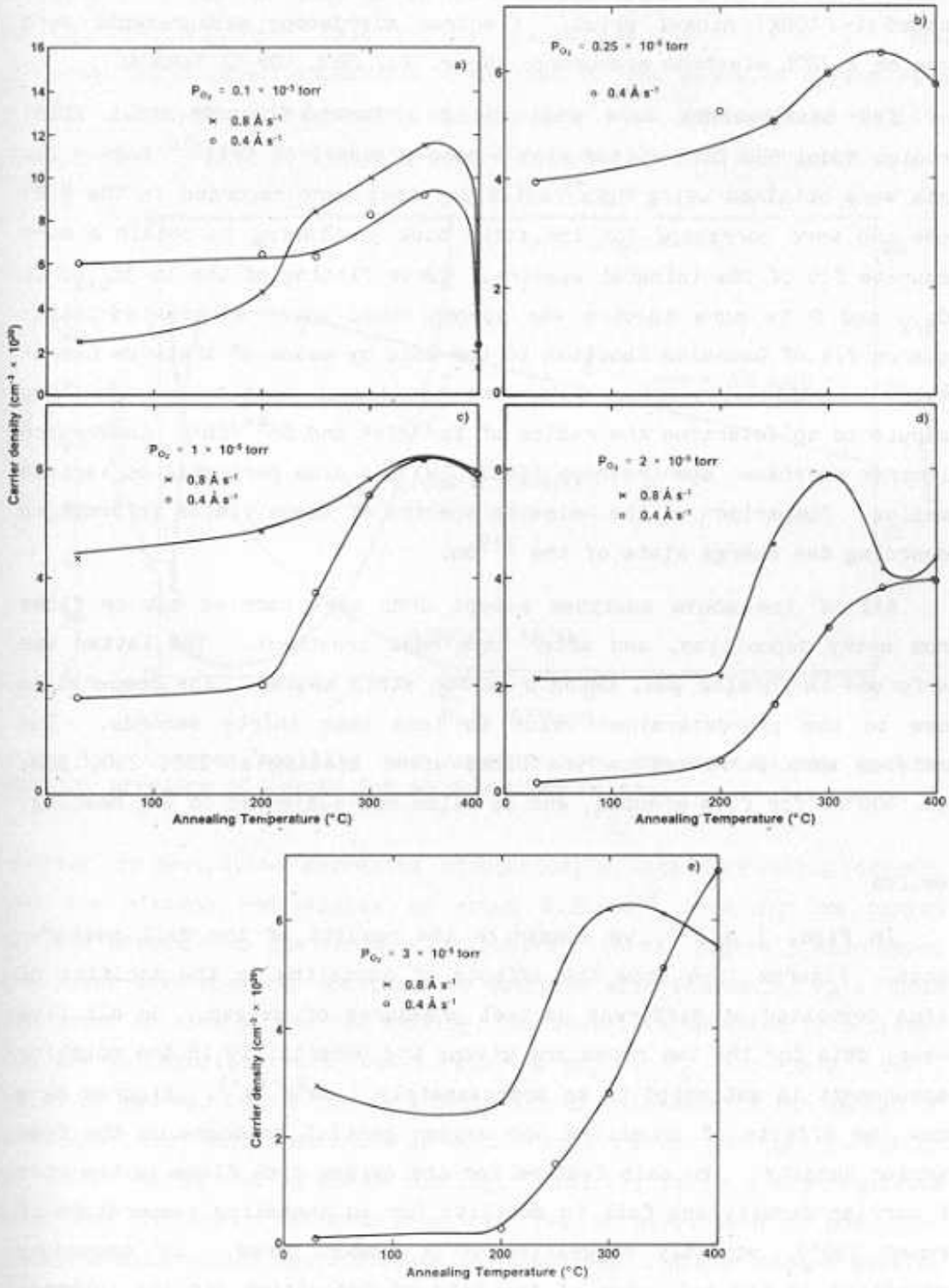

Fig. 2 a-e: Carrier concentration against annealing temperature for various partial pressures of oxygen and deposition rates.

The samples for electron-microscopy (TEM) were deposited on carbon-coated (~ 100Å) nickel grids. Electron microscopy measurements were done on a JEOL electron microscope (Model No. JEOL 100 CX TEMSCAN).

XPS measurements were made using a Perkin-Elmer/Physical Electronics Model 550 ESCA system with a base pressure of 5×10^{-10} torr. The data were obtained using MgKα radiation; they were recorded in the N(E) mode and were corrected for inelastic back scattering to obtain a more accurate fit of the integral spectra. Curve fitting of the In $3d_{5/2}$, Sn $3d_{5/2}$ and O 1s core spectra was accomplished using a weighted-least-squares fit of Gaussian function to the data by means of stepwise Gauss-Newton iterations. Areas under the individual components were then calculated to determine the ratios of In^{3+}/In° and Sn^{4+}/Sn° Conversion electron Mössbauer spectroscopy (CEMS) (9) was also performed on various samples. Comparison of the emission spectra of these yields information regarding the charge state of the ^{119}Sn.

All of the above analyses except CEMS were carried out on films from every deposition, and after each heat treatment. The latter was performed in forming gas, using a carbon strip heater. The temperature rose to the pre-determined value in less than thirty seconds. The analyses were performed on the films after heating at 200, 250, 300, 350, 400°C, for five minutes, and on films not subjected to any heating.

Results

In Figs. 1 and 2, we summarize the results of the Hall measurements. Figures 1a-e show the effects of annealing on the mobility of films deposited at different partial pressures of oxygen. In all five cases, data for the two rates are given; the uncertainty in the mobility measurement is estimated to be approximately 1 $cm^2V^{-1}s^{-1}$. Figures 2a-e show the effects of annealing and oxygen partial pressure on the free carrier density. The main feature for the oxygen rich films is the rise of carrier density and fall in mobility for an annealing temperature of around 250°V, possibly suggestive of a common cause. Of secondary importance is the influence of the rate of deposition and its interaction with the oxygen partial pressure. The carrier density is always greater for the faster rate but the mobility has a cross-over somewhere between $1\text{-}2 \times 10^{-5}$ torr. This suggests that the oxygen has at least two roles; we shall discuss this later. Figure 3 shows another representation of the electrical data of unannealed films. For the oxygen defi-

cient films, the mobility shows an opposite trend with increasing annealing temperature. That is, it starts low (~4-7 $cm^2\ V^{-1}s^{-1}$) and finishes at a level comparable with that of the annealed oxygen rich films. The general features of this are that the optimum mobility occurs at an oxygen partial pressure of about $1.00x10^{-5}$ torr; the

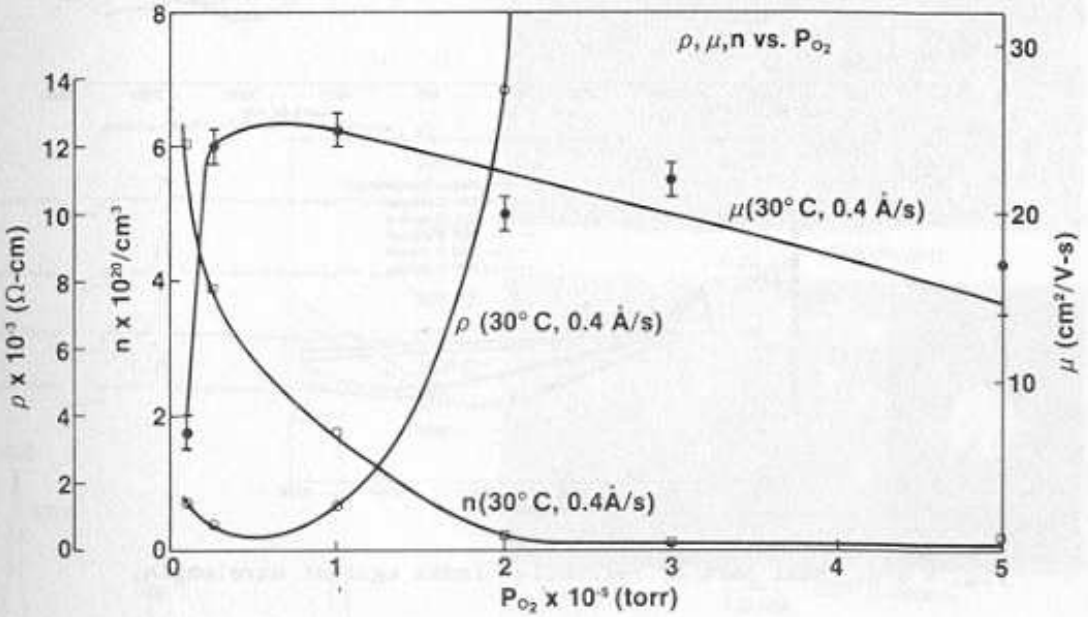

Fig. 3: Carrier mobility and concentration and resistivity against partial pressure of oxygen for as-deposited films.

carrier concentration decreases monotonically with increasing oxygen; and the minimum resistivity is about $6.25x10^{-4}$ Ω-cm for an oxygen partial pressure in the range $0.25\text{-}1.00x10^{-5}$ torr. Figure 3 also makes the point that mobility continues to decrease with increasing P_{O_2}. From the point of view of the resistivity, the lowest value actually achieved (in the as-deposited case) was $6.7x10^{-4}$ Ω cm, for $P_{O_2} = 0.25x10^{-5}$ torr. This, of course, is not the only criterion of relevance in the design of a window-layer which also has an active role in the junction formation of solar cells, and as an AR coating. Clearly, it is a pre-requisite that the ITO be as non-absorbing and free of dispersion as possible; these considerations would dictate the choice of a higher oxygen partial pressure. However, it would appear that there is also a gradual increase with time of the resistivity of films deposited at high values of P_{O_2}. Hence, it may be desireable to sacrifice some of the benefits of low dispersion and, with appropriate adjustment of the AR coating design, use lower values of P_{O_2}. Figures 4a-c show the dispersion of the real part of the refractive index for three representative values of

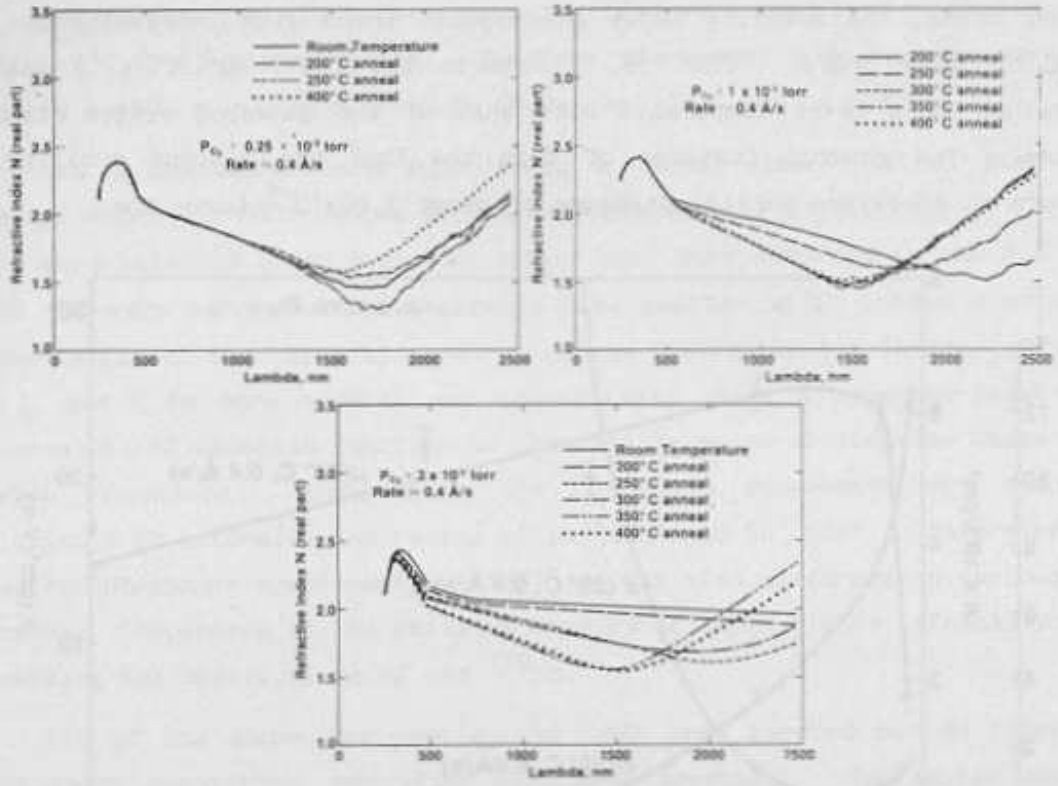

Fig. 4 a-c: Real part of refractive index against wavelength.

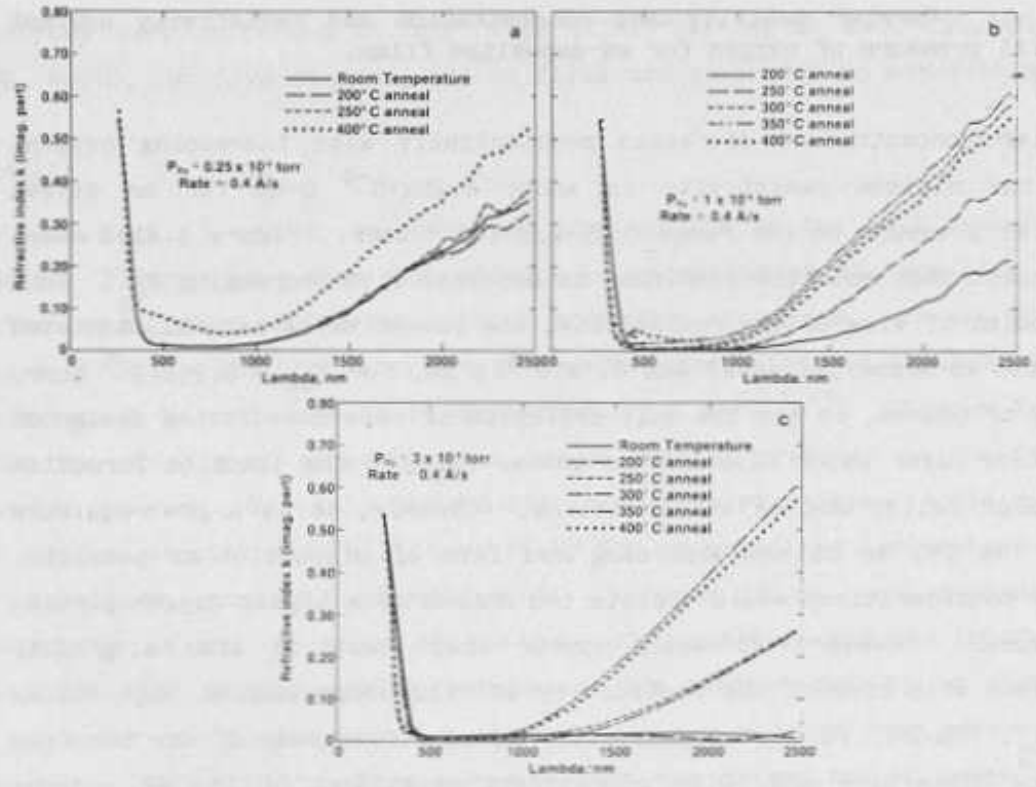

Fig. 5 a-c: Imaginary part of refractive index against wavelength.

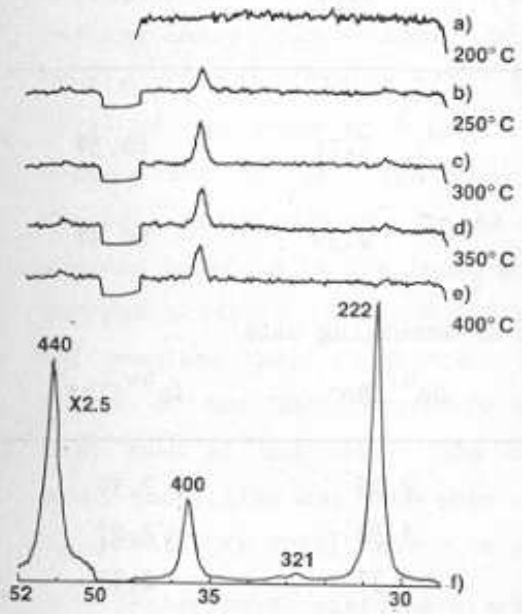

Fig. 6 a-f: X-ray diffraction spectra at various stages of annealing for a representative film: Fig. 6-f is the spectrum for In_2O_3 powder.

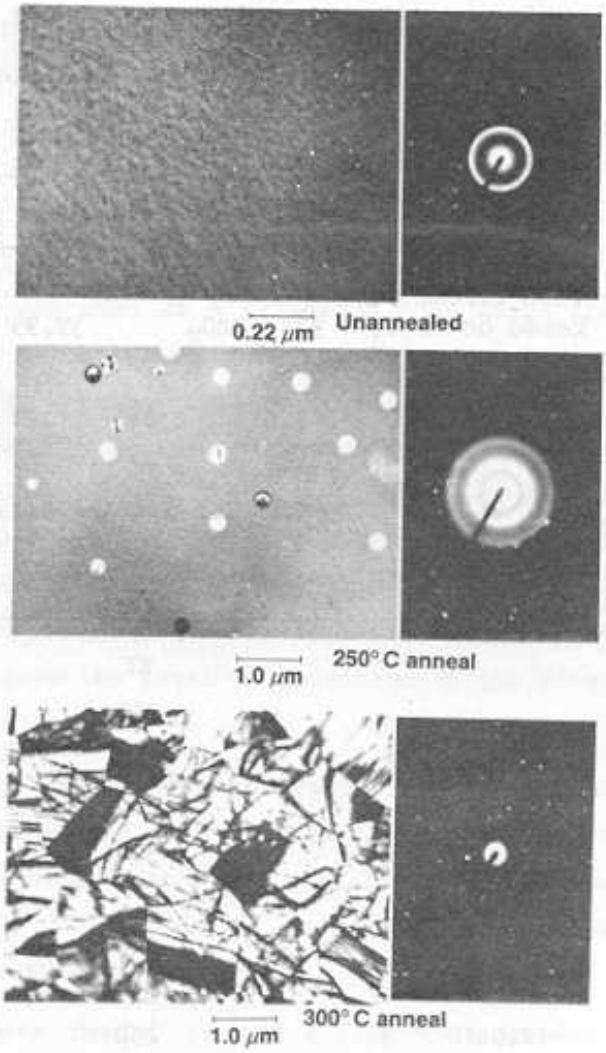

Fig. 7: Transmission electron micrographs and electron diffraction patterns for a typical film at different stages of annealing.

Table I: XPS Elemental Survey

P_{O_2}	Rate	$\bar{X}_{In}$	$\bar{X}_{Sn}$	$\bar{X}_{O}$
0.25	0.4	39.24	2.34	58.42
0.25	0.8	36.96	2.34	60.70
1.0	0.4	38.12	2.20	59.68
1.0	0.8	38.10	2.26	59.64
2.0	0.4	38.14	2.28	59.58
2.0	0.8	38.02	2.34	59.64
3.0	0.4	36.96	2.34	60.78
3.0	0.8	37.36	2.30	60.44
Theoretical values based on In_2O_3 + 9 m/o SnO_2		37.95	1.71	60.34
Theoretical values based on In_2O_3 + 12.5 m/o SnO_2		37.21	2.33	60.47

Table II: XPS Analysis of Annealing Data

Pressure (torr)	Anneal Temp (°C)	Sn^{4+}/Sn°	In^{3+}/In°
0.25×10^{-5} ($0.4\ A\ s^{-1}$)	RT	2.05	2.30
	200	3.32	2.27
	250	3.37	2.53
	300	3.42	2.64
	350	3.51	2.75
2.0×10^{-5} ($0.4A\ s^{-1}$)	RT	3.03	2.64
	200	3.26	2.60
	250	3.53	2.50
	300	3.57	2.53
	350	3.5C	2.52

P_{O_2} and after each annealing period. Figures 5a-c show the equivalent data for the imaginary part of the refractive index. As with the electrical data, there are no major changes until an annealing temperature of 250°C is reached. Also, at higher values of P_{O_2} the dispersion of both N and k becomes minimal.

The X-ray diffraction data showed that the films were quasi-amorphous before annealing but began to show significant structure after annealing at 250°C or above. In fact, above 300°C there was usually some loss of structure. In Figures 6a-e we show one set of data illustrating these observations. Diffraction was also performed on a powder sample of In_2O_3 (Figure 6f). Since the particle size of this was typically of the order of 1 μm, it was used as a reference from which the grain sizes in the films could be estimated. It should be noted that the only peaks observed in the diffraction spectra of the films, corresponded to those in the In_2O_3 powder spectrum; no peaks corresponding to various possible Sn/O compounds were found although their absence does not preclude their existence. Since the films were extremely thin, the volume of the Sn/O compounds would have been very small and not more than 9m/o of the total (the composition of the target). Hence such small quantities may have been below the level of detection of the X-ray equipment. We shall return to this point.

Transmission electron micrographs and the corresponding diffraction patterns are shown in Fig. 7 for a film deposited at $P_{O_2} = 3\times10^{-5}$ torr at several stages of annealing. These were entirely typical of films deposited at the other oxygen partial pressures; the key feature being the pronounced recrystallization between 250-300°C.

The XPS data have also been useful in clarifying this aspect. Table 1 shows the elemental survey of In, Sn and O, expressed in atomic percentages. The data at each oxygen partial pressure have been averaged from the XPS surveys of that film after each annealing step; since it was found that the latter had no systematic effect on the compositions. Also shown are the theoretical estimates of the atomic compositions based on the target composition; nominally 91 m/o In_2O_3:9 m/o SnO_2. However, it can be seen that the observed tin concentration was somewhat greater than that calculated, thus implying enrichment of the target. Therefore, an estimate of the probable proportion of tin was made and this corresponded to 12.5 m/o SnO_2. The theoretical values of the atomic concentrations of indium and oxygen have been recalculated on this basis.

It can be seen that the theoretical and observed compositions agree for an oxygen partial pressure of 3×10^{-5} torr. In general, the lower pressure and/or faster rates gave oxygen deficient films. Table II shows the ratios of Sn^{4+}/Sn^{o} and In^{3+}/In^{o} as a function of annealing temperature measured by XPS, for a high and a low pressure oxygen sample. The key point is that the ratios both increase for the low oxygen film and show little or no change for the high partial pressure.

Studies of the chemical composition have also been made using Mossbauer spectroscopy. This technique is capable of distinguishing whether the tin in the film appears as Sn^{2+} or Sn^{4+}. In the present case we have obtained a signal only from Sn^{4+} even after a very prolonged period of spectrum accumulation using a relatively thick sample (3500 A) as shown in Fig. 8.

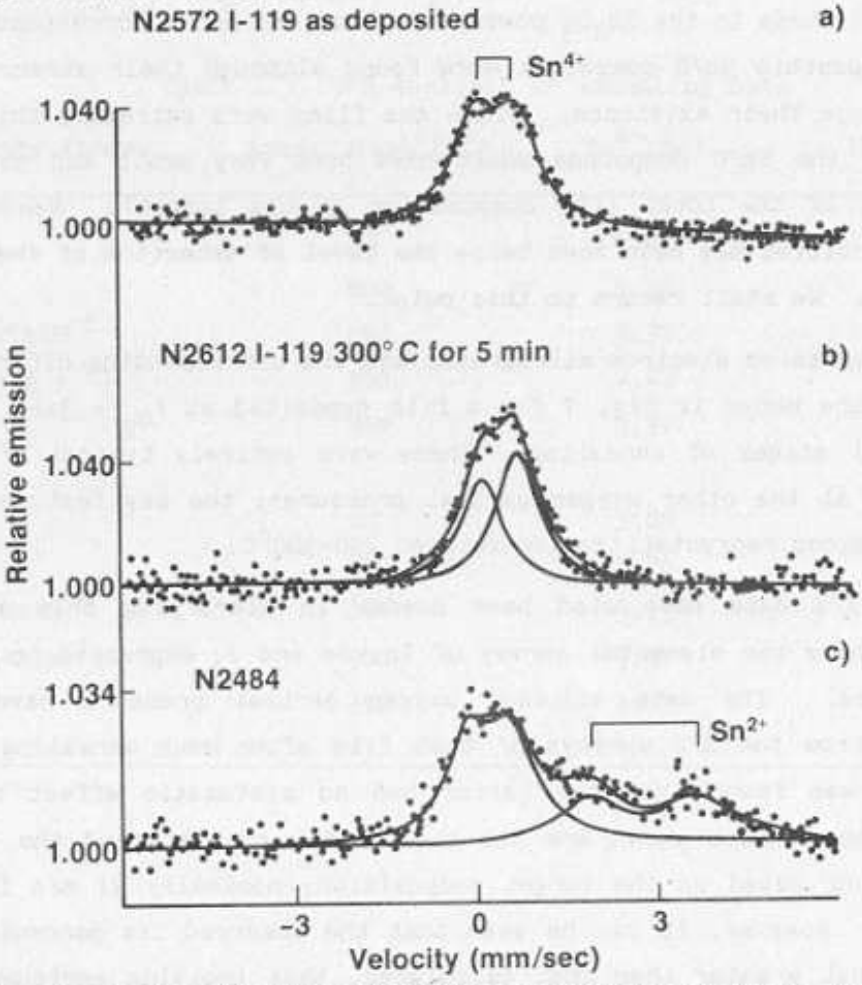

Fig. 8: Conversion Electron Mossbauer Spectrosocpy (CEMS) data illustrating the presence of only Sn^{4+} in the ion-beam deposited film I-119 (Fig. a and b). Figure c is provided to illustrate a spectrum where both Sn^{4+} and Sn^{2+} are present (This ITO film prepared by reactive RF sputtering).

Discussion

i) Structure and Composition.

There appeared to be no crystallinity evident in the films until they had been annealed in forming gas for five minutes at 250°C. The first evidence of crystallinity was a small, relatively wide, In_2O_3 <400> peak. With progressive annealing, this grew in height and decreased in half-width indicating increased orientation and grain size. The half width of the <400> peak for the 1 μm size powder shown in Fig. 6f, is actually greater than that of the corresponding peak for films annealed at 300°C or greater. Hence, the estimated grain size of these films (using the Debye-Scherrer formula) is 1.5-2.0 μm. It should be noted that the <222> and <440> peaks of Fig. 6f were observed to be of very low intensity in the film spectra indicating a strong <400> preferred orientation. No peaks corresponding to the expected Sn/O phases were found for these films of approximately 650 A thickness. The only difference between these and films of about 3500 A thickness, was that the latter showed a much stronger <222> orientation. However, once again, no Sn/O phases were found. The <400> preferred orientation for the thin films is distinct from the observations of other workers (10) and maybe a consequence of the annealing schedule or the relatively low film thickness. The TEM data also show that the as-deposited films are essentially amorphous although micro-crystalline may be a better description. After annealing at 250°C, circular crystallites of about 2500 A can be seen against the amorphous background and the diffraction pattern showed spots on diffuse rings. At 300°C widespread grain growth has taken place and the diffuse diffraction rings have disappeared. The grain size can be seen to be about 1.0-2.0 μm, in agreement with the X-ray diffraction data. No further grain growth or increase in preferred orientation occurred at higher annealing temperatures.

Figure 9 shows graphically the XPS data of Table II. This refers to the change in the ratio (R) of the area under the peak associated with the Sn^{4+} state, to that associated with the Sn° state, as a function of annealing temperature. A similar, although smaller, change was found for the In^{3+}/In° states. The effect was greatest for films deposited at a low partial pressure of oxygen and since it is known from the quantitative elemental survey that the absolute concentrations of

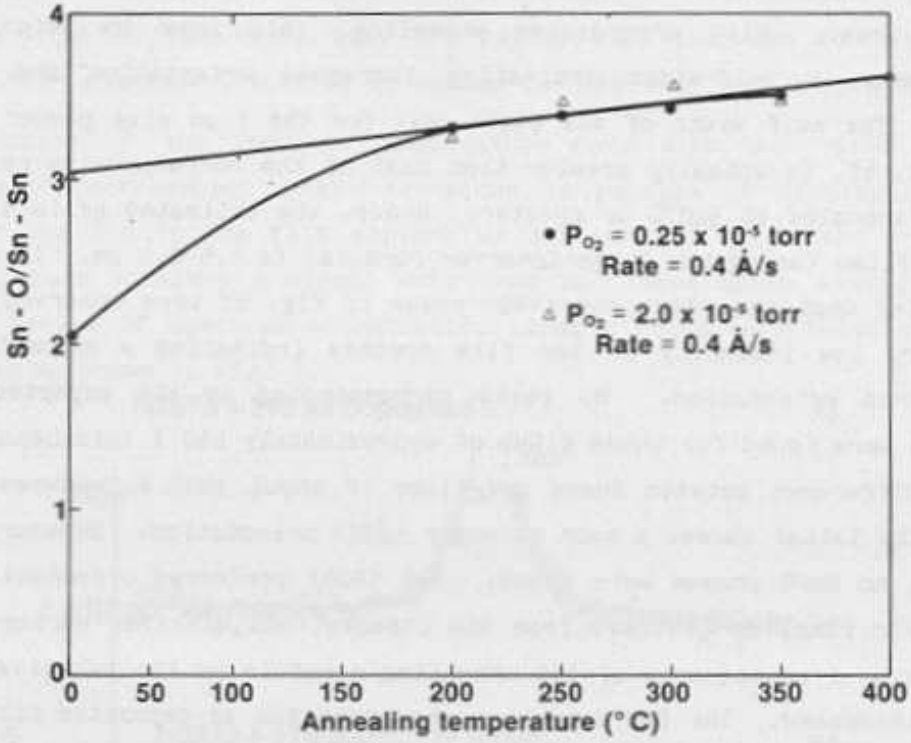

Fig. 9: Ratio of Sn^{4+} to Sn° against annealing temperature for high and low partial pressure of oxygen, obtained from XPS data.

Sn, In and O do not change with annealing, it seems clear that a redistribution of the oxygen takes place. One possible explanation is that the film as a whole consists mainly of In_2O_3, In_2O_3 with oxygen vacancies (In_2O_{3-y}), and both of these species in relatively close proximity to bonded or unbonded Sn atoms. With annealing, it is possible that oxygen redistributes, particularly from grain boundaries, and causes compensation of the oxygen vacancies, together with allowing grain growth. In addition, it is possible that most of the Sn atoms become 'activated' so that they dope the In_2O_3 substitutionally. Hence the overall effect will be an improvement in the order of the film and

an increase in the electrical activity of the tin. The data from Mossbauer spectroscopy shows that there is only evidence of Sn^{4+} without any Sn^{2+}. This would be consistent with the above model and with the X-ray data showing the absence of Sn/O compounds i.e., the Sn is never associated with oxygen alone; it is always in the presence of both In and oxygen, so its charge state is unchanged with the addition of an extra oxygen atom although a more ordered In_2O_3:Sn is formed. We shall refer to the structural model again in the context of the electrical and optical changes which occur with annealing.

ii) Electrical properties.

In this section we shall first discuss the expected carrier concentrations for annealed and unannealed films. We shall then consider the expected mobilities and the factors which limit mobility.

The target itself consists of (1-x) moles of In_2O_3 and x moles of SnO_2. When the target is sputtered not all of its oxygen is necessarily incorporated in the film which will therefore be oxygen deficient unless an additional supply is available from the sputtering gas. Assuming, for the moment, that this is so, then the film composition may be expected to be similar to that of the target. With annealing, however, we assume that the tin substitutes for indium and acts as a singly ionized donor. Therefore films deposited in a partial pressure of oxygen such that stoichiometric grains are formed, will have a low carrier concentration before annealing because there will be no oxygen vacancies, only partially activated (i.e., substitutional) Sn, plus carrier trapping by excess oxygen at grain boundaries. After annealing, and complete activation of all the Sn, it would be possible in principle to achieve a carrier concentration of 3.6×10^{20} cm^{-3} (based on the XPS data which indicated 2.3 $^{a}/_{o}$ Sn).

Films deposited at a low partial pressure of oxygen exhibit a much higher carrier density before annealing than those described above because of there being a significant concentration, up to 2 $^{a}/_{o}$, of oxygen vacancies, plus the possible contribution from partially activated Sn. It is also probable that some oxygen resides at grain boundaries where it may act as a carrier trap. Upon annealing, and the removal of the effects grain boundary oxygen, the latter is redistributed throughout the film, the density of oxygen vacancies is reduced, the tin is further activated, and grain growth takes place. The net

effect of all this is a better ordered film with an increase in carrier density. Films deposited at a high partial pressure of oxygen exhibit a relatively low carrier density before annealing because of extensive carrier trapping at the grain boundaries by excess oxygen. The carrier concentration in this case is due mainly to the partially activated Sn. Upon annealing, the excess oxygen at the grain boundaries is removed (i.e., either redistributed througout the film or removed completely from it) grain growth occurs, and the Sn is activated more completely. The increase in the carrier concentration is therefore due to a reduction in the carrier trapping and the addded contribution of substitutional Sn. On the basis of the above arguments and the model of oxygen redistribution the maximum carrier concentration possible would be $3.6\times10^{20}cm^{-3}$ (due to the substitutional Sn) plus 3×10^{20} cm^{-3} (per atomic percent of doubly ionized oxygen vacancies). Hence, for a film with 1 $^{a}/o$ vacancies (i.e., $P_{O_2} \approx 1\times10^{-5}$ torr) we expect the maximum carrier density to be 6.6×10^{20} cm^{-3}, and for 2 $^{a}/o$ (i.e., 0.25×10^{-5} torr), it would be 9.6×10^{20} cm^{-3}. These estimates agree extremely well with our observation. Figure 10 shows a plot of ℓn (carrier density) vs $1/T_a$ where T_a is the annealing temperature. This gave an activation energy of about 0.3 eV (0.13 k cal $mole^{-1}$) similar to that reported by Hoffman et al (11). Since this value is far lower than that of the heat of formation of SnO_2, SnO or In_2O_3, the above activation energy may be that associated with the diffusion of oxygen through the film to complete the In_2O_3: Sn lattice.

We shall now consider the variation of mobility with annealing and oxygen partial pressure, in terms of the oxygen re-distribution and evolution model. Firstly, those films in which the grains (or microcrystallites) consist of near stoichiometric material will have their mobility limited by grain boundaries plus any scattering due to excess oxygen residing there. With annealing and the elimination of the latter mechanisms, the mobility becomes limited by the relatively large concentration of activated tin plus any remaining vacancies. The net effect is a reduction in mobility thus implying the dominance of ionized Sn. This argument also applies to films deposited at higher partial pressures.

The mobility of films deposited with a deficiency of oxygen in the grains is limited, before annealing, by grain boundary scattering, by scattering due to oxygen vacancies and such active Sn as exists before

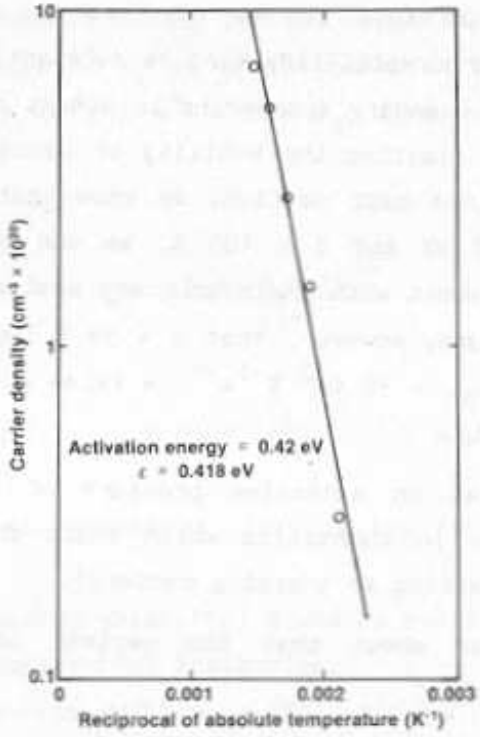

Fig. 10: Arhenius plot of carrier density; activation energy = 0.42 eV.

annealing. When the films are annealed the grain boundary mechanism is eliminated but the vacancies are now only partially eliminated and particularly the larger contribution from oxygen vacancies. These two mechanisms now more than counteract the additional scattering due to the more completely activated Sn, so that the net effect is an increase in mobility. We shall now examine these mechansims semi-quantitatively. Grain boundary scattering limited mobility can be expressed by (4)

$$\mu_g = \mu_o T^{-\frac{1}{2}} \exp(-\phi/KT) \qquad (1)$$

with

$$\mu_o = \left(\frac{d^2}{2\pi m^* K}\right)^{\frac{1}{2}}$$

For stoichiometric films where the only additional scattering mechanism would be expected to be due to the relatively small quantity of active Sn, this equation should apply. Equation (1) exhibits a maximum at a temperature $T_m = \frac{2\phi}{K}$ (K). Although we have observed that the mobility is virtually independant of temperature, there is slight evidence of a broad maximum around T=70K (although the data are by no means sufficiently convincing to plot $\ln \mu T^{\frac{1}{2}}$ - 1/T) which would imply $\phi \simeq$ 0.007 eV. The magnification used in the electron microscopy was 50,000 so

that the lower limit of resolvable feature size is about 100 Å. Since no features as large as this can be resolved we conclude that the average size of the microcrystallites must be substantially less. Hence we conclude that grain boundary scattering is almost certainly at least partly responsible for limiting the mobility of uannealed films. From optical measurements (see next section) we know that $m^* = 0.4\ m_e$, so that taking $\phi = 0.007$ eV and $d = 100$ Å, we can calculate that the maximum mobility consistent with grain boundary scattering is about 110 $cm^2V^{-1}s^{-1}$. If we assume, however, that $d = 30$ Å (comparable with the mean free path) then $\mu_{gb} = 35\ cm^2\ V^{-1}s^{-1}$; a value which would severely limit the total mobility.

Films deposited at an excessive pressure of oxygen, will also contain neutral oxygen in quantities which could affect the mobility adversely (as well as acting as trapping centers).

Erginsoy (12) has shown that the neutral impurity scattering mobility would be given by

$$\mu_o = \frac{8\pi^3\ m^*\ e^3}{20\varepsilon_o\varepsilon_r n_o h^3} \qquad (2)$$

with n_o being the density of neutral impurity atoms. For example using values of $m^* = 0.4\ m_e$ and $\varepsilon_r = 4.00$ (see Section (iii) of Discussion) we find that $\mu_o = 45\ cm^2V^{-1}s^{-1}$ for $n_o = 4\times10^{20}\ cm^{-3}$. Hence for systems such as ITO which may well have a very large density of neutral impurities, the latter would be expected to reduce the mobility significantly even though the mechanism was first formulated in the context of low temperature effects.

Films deposited in a relatively low partial pressure of oxygen will exhibit scattering by the doubly ionized vacancies. At annealing temperatures greater than 200°C, the carrier density increases sharply because of tin activation. Hence these two species can be expected to act as ionized scattering centers. For a degenerate semiconductor, the mobility, as defined by ionized impurity scattering is given by (13)

$$\mu_i = \frac{3\ h^3\ (\varepsilon_o\varepsilon_r)^2\ n}{16\pi^2 e^3\ m^{*2} f(x) n_i} \qquad (3)$$

where

$$f(x) = \ln(1+x) - \frac{x}{1+x}, \text{ and } x = \tfrac{1}{2}\left(\frac{h}{e}\right)^2\left(\frac{\varepsilon_o\varepsilon_r}{m^*}\right)\left(\frac{3n}{8\pi}\right)^{1/3}$$

If we assume, for example, doubly ionized oxygen vacancies (1), then $n = 2n_i$ and the dependence of μ_i on n_i is contained in the expression for $f(x)$. If we use $\varepsilon_r=4$ and $m^* = 0.4\ m_e$, then $x=4.081\times10^{-10}\ n^{1/3}$ (n measured in m^{-3}) and

$$\mu_i = \frac{0.3290 \times 10^{-4}}{f(x)}$$

e.g., for $n=6\times10^{26}\ m^{-3}$, $\mu_i = 0.00041\ m^2V^{-1}s^{-1}$ i.e., $4.1\ cm^2V^{-1}s^{-1}$.

Hence, the three mechanisms limiting the mobility in these films are:

i) Grain (or microcrystallite) boundary scattering.
ii) Neutral impurity (Sn) scattering.
iii) Ionized impurity scattering (Sn^{4+} and V_o^{2+}).

In Table III, we show the relative magnitudes for each of these. The total number of Sn atoms is taken as $4\times10^{20}\ cm^{-3}$; equivalent to 2.3 a/o Sn. That is $n_o + n_i = 4\times10^{20}\ cm^{-3}$. Mobilities are calculated for three different concentrations of oxygen defects.

Table III: Calculated Mobilities

n_i ($\times10^{20}$ cm^{-3})	μ_i^{Sn} ($cm^2V^{-1}s^{-1}$)	n_o $\times10^{20}$ cm^{-3})	μ^o ($cm^2V^{-1}s^{-1}$)	$\mu_{Sn}^{4+,o}$ ($cm^2V^{-1}s^{-1}$)	$\mu_{Sn,gb}$ ($cm^2V^{-1}s^{-1}$)
0	∞	4	45	45	20
1	11.6	3	60	10	8
2	7.7	2	90	7	6
3	6.1	1	180	6	5
4	5.3	0	∞	5	5

μ_{gb} = 35 $cm^2\ V^{-1}s^{-1}$ $\quad \mu_{V_o}$ (2 a/o) = 3.0 $cm^2\ V^{-1}s^{-1}$

μ_{V_o} (1 a/o) = 4.5 $cm^2\ V^{-1}s^{-1}$ $\quad \mu_{V_o}$ (3 a/o) = 2.4 $cm^2\ V^{-1}s^{-1}$

Using the table, it is possible to demonstrate that the trends of the mobility with annealing are correct,but the absolute magnitudes are generally too low. This is not uncommon in modelling mobility, particularly in situations where high impurity concentrations are involved; the reason given usually involving charge screening of the scattering centers. Hence, in this case, we conclude that the scattering power of the ionized Sn and oxygen vacancies is not as great as predicted using equations 2 and 3. In practice, all films tended to a value of about 10-14 $cm^2v^{-1}s^{-1}$ after annealing, irrespective of the initial oxygen partial pressure, as predicted.

iii) Optical Properties

Firstly, we shall examine the data concerned with the optical analyses and in particular concentrate on the regions near the fundamental edge and the plasma edge. We have previously processed data near the plasma edge for films deposited on borosilicate glass substrates (8) using the Drude theory and the films discussed here behave very similarly. The basic relationships used are:

$$\varepsilon^* = (N - ik)^2 = \varepsilon_\infty - \frac{ne^2}{\varepsilon_o m^*(\omega^2 - \omega/\tau)} \qquad (4)$$

from which we have $$\varepsilon^* = \varepsilon' - i\varepsilon'' \qquad (5)$$

where $$\varepsilon' = N^2 - k^2 = \varepsilon_\infty - \frac{ne^2}{\varepsilon_o m^*(\omega^2 + 1/\tau^2)} \qquad (6)$$

and $$\varepsilon'' = 2Nk = \frac{ne^2}{\varepsilon_o m^* \omega\tau(\omega^2 + 1/\tau)} \qquad (7)$$

Hence, by combining equations 6 and 7 we can obtain

$$\varepsilon' = \varepsilon_\infty - \omega\varepsilon''\tau \qquad (8)$$

Thus, a plot of ε' against $\omega\varepsilon''$ should be a straight line (at least in that part of the spectrum where free electron absorption is evident) of slope τ. All the above symbols are defined in the nomenclature. The

plasma frequency is defined as the point at which $\varepsilon' = 0$ and, since $\omega >> 1/\tau$, this can be obtained from equation 6, viz.

$$\omega_p = \left(\frac{ne^2}{\varepsilon_\infty \varepsilon_o m^*}\right)^{1/2}$$

Hence
$$\varepsilon' = \varepsilon_\infty \left(1 - \frac{ne^2}{\varepsilon_o \varepsilon_\infty m^* (\omega^2 + 1/\tau^2)}\right) \qquad (9)$$

or
$$\varepsilon' = \varepsilon_\infty \left(1 - \frac{\omega_p^2}{\omega^2 + 1/\tau^2}\right) \qquad (10)$$

so that having obtained τ we can plot ε' against $(\omega^2 + 1/\tau^2)^{-1}$ to obtain a straight line of intercept equal to ε_∞ and slope $= -\varepsilon_\infty \omega p^2$. In general, films which had either been deposited at low values of P_{O_2} or had been annealed at 250°C and above, showed a very pronounced decrease in ε' although on no occasion did ε' become negative. This may be due to the films being far less in thickness than the typical skin-depth at these frequencies, i.e., $\delta = \left(\frac{4\pi k}{\lambda}\right)^{-1} = 6\mu m$ and $\lambda = 1.5\ \mu m$) whereas the typical film thickness was substantially less than 0.1 μm. However, we have plotted several sets of data and derived values of ω_p from which we have also been able to estimate m^*. Figures 11 and 12 show the above plots, from which we derive $\tau = 2.9 \times 10^{-15}$ sec., $\omega_p = 6.3 \times 10^{14} sec.^{-1}$, $\varepsilon_\infty = 4.004$, $m^* = 0.30\ m_e$ (for this film $n = 1.5 \times 10^{20} cm^{-3}$). As the annealing temperature was increased, there appeared to be a tendency for m^* to increase ($m^* = 0.54\ m_e$ at 300°C, $m^* = 0.72\ m_e$ at 400°C); however there was substantial scatter in the data and these results must be treated cautiously. Work is presently in progress to analyze the behavior of much thicker ITO films where the skin depth restriction is no longer problematic. However, in general the films appear to behave similarly to those of other workers, the origin of the relatively low mobilities being the main point of interest. Some information about scattering processes can be obtained from the variation of the absorption coefficient with wavelength in the near IR. In Fig. 13 we show a plot of log α against log λ which exhibits good linearity over the range 0.9 - 2 μm. The index of λ depends on the particular film studied and its annealing temperature, but was generally greater than 3.0. This is taken to be indicative of scattering by ionized impurities (14) although it should be noted that the index changes considerably outside the specified wavelength range. This is probably indicative of other scattering mechanisms. However, the conclusion that impurities are

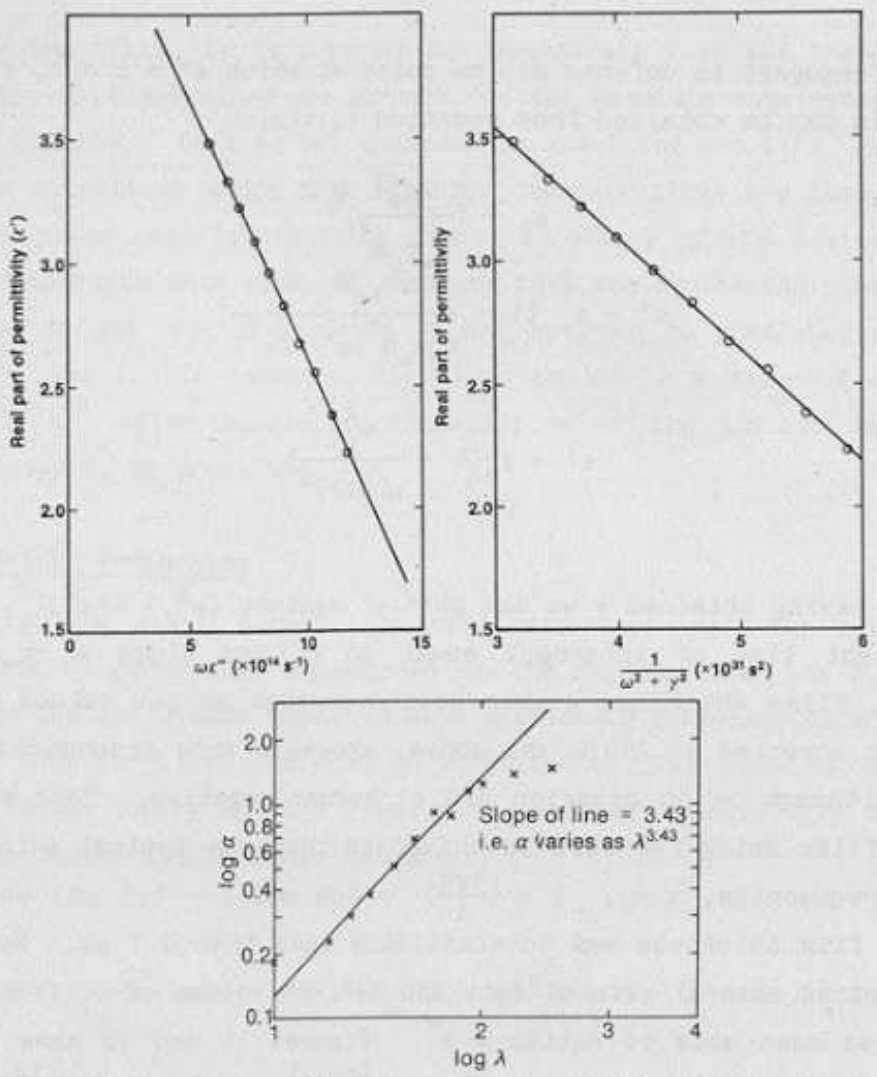

Fig. 11: Real Part of permittivity against ωε'' (see text for details)

Fig. 12: Real Part of permittivity against $(\omega^2 + \gamma^2)^{-1}$. This plot yields effective mass and ε_∞.

Fig. 13: Log of absorption coefficient against log wavelength. The index of 3.43 is indicative of ionized impurity scattering.

responsible for the limited mobilities is in agreement with the work of Hamberg et al (2). Only those films which showed a pronounced decrease in ε' (i.e., a plasma edge) showed log α proportional to K log λ (with K > 3.0). Those films which had been deposited at $P_{O_2} > 1 \times 10^{-5}$ torr and which had not been annealed at 250°C or greater, had very low absorption coefficients up to 2.5 μm, and did not conform to this behavior. Since these also exhibited no minimum in ε' (i.e., no free electron absorption effects) it is reasonable to suppose a common cause, i.e., ionized impurities, are responsible for the increase in carrier density and for near IR optical scattering (as also demonstrated by electrical measurements). Near the fundamental edge we, as many other groups,

observe that the optical gap increases in direct proportion to $n^{2/3}$, i.e., the Moss-Burstein shift. In Fig. 14, we show the variation for all the films after each of the annealing steps. Although there is a very substantial scatter of the data, the correlation coefficient of 0.8 is rather convincing. The reduced effective mass based on the aggregated data is $m_{cv} = 0.38\ m_e$. It is interesting that if we consider individual films deposited at different values of P_{O_2} and different rates, the correlation coefficients are generally 0.95 or greater, even though there were only six data points per film. Typically, the values of m_{cv} lay in the range (0.3-0.4) m_e although one film (the data from which showed extremely large scatter) showed $m_{cv} = 0.62\ m_e$. As with the effective mass, the intercepts on the energy axis, corresponding to the undoped semiconductor, lay in a relatively small range between 3.55-3.75 eV (which agrees with the findings of other groups) implying that the fundamental material is In_2O_3 ($E_{go} = 3.75$ eV).

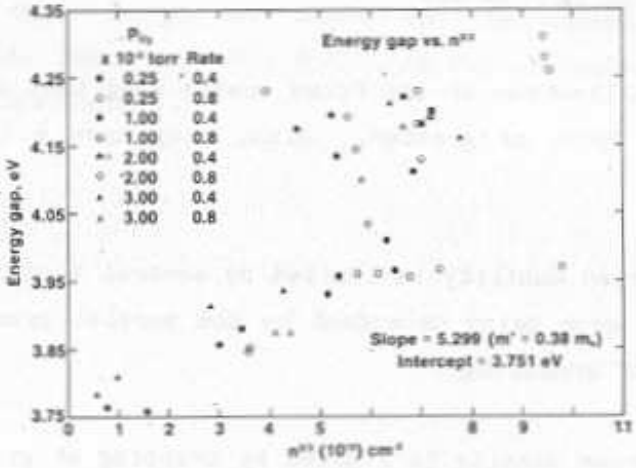

Fig. 14: Optical gap as a function of free carrier density.

In our case, we have determined the energy of the direct transitions from plots of $(\alpha h\nu)^2 \sim h\nu$. These plots were linear only over a comparatively limited range of about 0.5 eV and so significant errors may have arisen in the extrapolation of the linear portions to the $h\nu$ axis. We believe that this may be responsible for much of the scatter in the Moss-Burstein plots. Nevertheless, the values of m^* and Eg_o are in excellent agreement with those reported elsewhere (see, for example the review by Chopra (1)). We do not have any convincing evidence to support the data of Ohaha et al (15) that the value of m_{cv} (i.e., the

values of m^* inferred from the Moss-Burstein data) is at all different from that of the free electrons (i.e., the values inferred from the data near the plasma edge). Thus, we do not need to invoke the concept of a negative effective mass being associated with the valence band (15). Nor do we need to invoke electron/electron scattering as used by Hamberg et al (3) to remove the latter requirement. It is merely necessary to assume m_v is too large to have any influence on the reduced effective mass, m_{cv}, since $m_{cv} = m^*$.

iv) Conclusions

The principal conclusions which can be drawn from this work are as follows;

1) Although the sputtering target consists of mixed oxides of In_2O_3 and SnO_2, there is no evidence for any Sn/O phases in the films, before or after annealing. Furthermore the Sn is never found in the Sn^{2+} state but only exists as Sn^{4+} or Sn°.

2) Recrystallization of the films occurs when they are annealed in forming gas at 250°C or greater. Also, they have a <400> preferred orientation.

3) The carrier mobility is limited by several mechanisms the relative effects of each being dependent on the partial pressure of oxygen and the extent of annealing.

4) The carrier density is limited by trapping at grain boundaries, the electrical activity of the Sn, and the tolerable level of oxygen vacancies.

5) Annealing causes a redistribution of oxygen within the films which leads to improved composition and structure, plus an increase in the Sn activity.

6) For unannealed films the lower limit in resistivity is 6.25×10^{-4} Ω cm, and for annealed films it is 1.66×10^{-4} Ω cm. It may be possible to reduce these values if the strong interdependence of mobility and carrier density could be reduced.

7) The dispersion of the optical constants is least for unannealed films deposited at relatively high partial pressures of oxygen.

8) For films deposited at low partial pressures of oxygen or, in general, annealed films, free electron effects always cause a plasma absorption edge in the near I.R. The effective mass of the charge carriers is about 0.4 m_e as calculated from the Drude model.

9) A shift of the fundamental optical gap occurs due to conduction band degeneracy. Analyzing the shift in terms of the Moss-Burstein model again implies a reduced effective mass of about 0.4 m_e.

Acknowledgements

This work was supported by Department of Energy contract number DE-AC02-83CH10093. The authors wish to thank Don Williamson for help with the Mossbauer spectroscopy, Kim Jones for the transmission electron microscopy, Keith Emery and Lynn Schilling for automated data acquisition and spectrophotometry.

References

1. K.L. Chopra, S. Major, and D.K. Pandya, Thin Solid Films, 102, 1 (1983).

2. I. Hamberg and C.G. Granqvist, Appl. Phys. Lett., 44, 721 (1984).

3. I. Hamberg, C.G. Granqvist, K.F. Berggren, B.E. Sernelius, and L. Engstrom, Phys. Rev. B., 30, 3240 (1984).

4. J.Y.W. Seto, J. Appl. Phys., 46, 5247 (1975).

5. V.K. Jain and A.P. Kulshneshtha, Solar Energy Mat. 4, 151 (1981).

6. J. Szczyrbowski, A. Dietrich, and H. Hoffman, Phys. Stat. Sol. (a), 69, 217 (1982).

7. T.J. Coutts and S. Naseem, Appl. Phys. Lett. 46, 164 (1985).

8. H. Aharoni, T.J. Coutts, T.A. Gessert, R.G. Dhere, and L.L. Schilling, J. Vac. Sci. Technol., A4, 428 (1986).

9. G.S. Collins, T. Kachonowski, N. Benczes-Koller and M. Pasternak, Phys. Rev. B, 19, 1369 (1979).

10. D.B. Fraser and H.D. Cook, J. Electrochem. Soc. 119, 1368 (1972).

11. H. Hoffman, A. Dietrich and J. Pickl, Appl. Phys. 16, 381 (1978).

12. C. Erginsoy, Phys. Rev. 79, 1013 (1950).

13. E. Conwell and V.F. Weisskoff, Phys. Rev. 77, 388 (1950).

14. R.A. Smith, "Semiconductors", Cambridge Univ. Press, Cambridge, 2nd Ed., 298 (1978).

15. Y. Ohata, F. Shinoki, and S. Yashida, Thin Solid Films, 59, 255 (1979).

Symbol List

P_{O_2}	oxygen partial pressure (torr)
μ_g	mobility due to grain boundary scattering ($cm^2\ V^{-1}s^{-1}$)
μ_o	pre-exponential factor in expression for grain boundary mobility ($cm^2\ V^{-1}s^{-1}\ K^{\frac{1}{2}}$), or neutral impurity limited mobility ($cm^2\ V^{-1}s^{-1}$)
T	absolute temperature (K)
K	Boltzmann's constant ($eV\ K^{-1}$)
d	grain (microcrystallite) size (cm)
m^*	effective carrier mass (gm)
m_e	free electron mass (gm)
ϵ_o	permittivity of free space ($farad\ m^{-1}$)
ϵ_r	relative permitivity
n_o	density of neutral impurity atoms (cm^{-3})
h	Planck's constant (eV s)
n	carrier density (cm^{-3})
n_I	density of ionized impurity atoms (cm^{-3})
μ_I	ionized impurity limited mobility ($cm^2\ V^{-1}s^{-1}$)
Tann	annealing temperature (K)
N	real part of refractive index
k	imaginary part of refractive index
μ	film mobility due to all scattering mechanisms ($cm^2\ V^{-1}s^{-1}$)
λ	wavelength (nm)
$R_\square$	sheet resistance (Ω per $\square$)
ω	$= 2\pi\nu$ = angular frequency (s^{-1})
ω_p	plasma frequency (s^{-1})
τ	electron relaxation time (s)
ϵ_∞	high frequency permitivity
ϵ'	real part of permitivity
ϵ''	imaginary part of permitivity
δ	$= \left(\frac{4\pi k}{\lambda}\right)^{-1}$ = skin depth (cm)
m_{cv}	reduced effective mass (gm)
α	$= 1/\delta$
ϕ	grain boundary potential barrier (eV)